Applied Catalysis B: Environmental 218 (2017) 600–610

Contents lists available at ScienceDirect

Applied Catalysis B: Environmental

journal homepage: www.elsevier.com/locate/apcatb

All-solid-state Z-scheme 3,4-dihydroxybenzaldehyde-functionalized Ga_2O_3/graphitic carbon nitride photocatalyst with aromatic rings as electron mediators for visible-light photocatalytic nitrogen fixation

Shihai Cao [a], Ning Zhou [a], Fenghua Gao [b], Huan Chen [a,*], Fang Jiang [a,*]

[a] Key Laboratory of Jiangsu Province for Chemical Pollution Control and Resources Reuse, School of Environmental and Biological Engineering, Nanjing University of Science and Technology, Nanjing 210094, China
[b] School of Environmental Engineering, Nanjing Institute of Technology, Nanjing 211167, China

ARTICLE INFO

Article history:
Received 17 April 2017
Received in revised form 16 June 2017
Accepted 5 July 2017
Available online 8 July 2017

Keywords:
All-solid-state Z-scheme
3,4-Dihydroxybenzaldehyde-functionalized Ga_2O_3/graphitic carbon nitride
Aromatic rings
Visible light photocatalysis
Nitrogen fixation

ABSTRACT

An all-solid-state Z-scheme heterojunction-structured photocatalyst, 3,4-dihydroxybenzaldehyde-functionalized Ga_2O_3/graphitic carbon nitride (Ga_2O_3-DBD/g-C_3N_4), was synthesized using a facile post-grafting strategy via Schiff base chemistry. It was proposed for the first time that aromatic rings served as electron mediators in the Z-scheme photocatalytic system. In addition, the aromatic rings were conducive to the formation of a well-developed combined interface between Ga_2O_3-DBD and g-C_3N_4, greatly improving the separation of electrons and holes. The Ga_2O_3-DBD/g-C_3N_4 exhibited a wide absorption range, high charge-separation efficiency and high redox potential, thus enhancing its activity and stability for visible-light photocatalytic nitrogen fixation. The reaction mechanism was demonstrated to be that O_2 was first reduced to H_2O_2, which was further oxidized to $^{\bullet}OH$; then, $^{\bullet}OH$ reacted with methanol to form $^{\bullet}CO_2^-$, which facilitated the reduction of N_2 to NH_3. This study demonstrates a simple and cost-effective approach to synthesize all-solid-state Z-scheme photocatalytic system using the aromatic rings, and this system exhibits great potential for practical applications of visible-light photocatalytic nitrogen fixation.

1. Introduction

Heterogeneous catalytic conversion of nitrogen from the atmosphere to ammonia has attracted great attention as it plays an important role in the development of modern industry and agriculture [1,2]. However, in addition to some natural nitrogen fixation by bacteria, all lifeforms rely on artificial nitrogen fixation mainly through the Haber–Bosch process, which requires high-energy inputs [3,4]. Therefore, the development of an efficient method with low energy consumption for nitrogen fixation under mild conditions is essential.

As a green and economical chemistry technology, photocatalysis shows great potential for nitrogen fixation [5–7]. Till date, various semiconductor photocatalysts have been reported for nitrogen photofixation under ultraviolet (UV) or visible-light irradiation, including BiOBr [8], WO_3 [9], Ga_2O_3 [10] and g-C_3N_4 [11]. However, low efficiency or poor stability limits the practical applications of photocatalytic nitrogen fixation [1]. It is difficult for a single-component photocatalyst to possess both a wide light-absorption range and high redox potential [12]. To overcome this limitation, various strategies have been employed to form specific stack architectures, including semiconductor–semiconductor (S–S) heterojunctions (e.g. $Ni_2P/Cd_{0.5}Zn_{0.5}S$ [13], TiO_2/CdS [14] and I–BiOCl/I–BiOBr [15]), semiconductor–metal (S–M) heterojunctions (e.g. Ag/$BiVO_4$ [16] Ag/BiOBr [17] and Pt/C_3N_4 [18]), semiconductor–carbon (S–C) heterojunctions (e.g. MoS_2/C_3N_4 [19] and WO_3/graphene [20]) and multicomponent heterojunctions (e.g. $V_2O_5/BiVO_4/TiO_2$ [21] and Ag nanowires–CdS–Au [22]). The interface connection pattern between the materials has impact on the morphology of the heterostructure and separation of photogenerated charge carriers, which affects the photocatalytic activity [23]. The photogenerated electron transfer models can be classified as heterojunction-type or Z-scheme photocatalytic systems [24]. The heterojunction-type photocatalytic system can inhibit the undesirable recombination of photogenerated charge carriers and greatly improve the photocatalytic activity. However, the decline of oxidizability and reducibility limits its practical application for

* Corresponding authors.
E-mail addresses: hchen404@njust.edu.cn (H. Chen), fjiang@njust.edu.cn (F. Jiang).

http://dx.doi.org/10.1016/j.apcatb.2017.07.013
0926-3373/

nitrogen fixation [25,26]. For the Z-scheme photocatalytic system, the photogenerated electrons and holes can be selectively separated, leading to a higher redox capacity [27,28].

Based on the type of electron mediators employed, Z-scheme photocatalytic systems can be divided into three types: photosystem–acceptor/donor–photosystem (PS–A/D–PS), photosystem–conductor–photosystem (PS–C–PS) and photosystem– photosystem (PS–PS) [24]. Among these systems, the all-solid-state Z-scheme photocatalytic systems (PS–C–PS and PS–PS systems) demonstrate a potential in practical applications. The noble metals (e.g. Au [29] and Ag [30]) are usually used as the electron mediators in the PS–C–PS systems [31]. However, the instability of noble metals and relatively high cost remarkably limits the practical applications of PS–C–PS systems. Therefore, it is important to develop a low-cost non-metal material with excellent conductivity to be used as the electron mediators in the PS–C–PS systems.

Inspired by the advantages of Z-scheme photocatalytic systems, a facile post-grafting strategy to design an all-solid-state Z-scheme heterojunction-structured photocatalyst, 3,4-dihydroxybenzaldehyde-functionalized Ga_2O_3/graphitic carbon nitride (Ga_2O_3-DBD/g-C_3N_4), has been developed in this paper. The grafting of Ga_2O_3-DBD nanoparticles (NPs) affects the electrical structure of g-C_3N_4, and the aromatic rings are conducive to forming a well-developed combined interface between Ga_2O_3-DBD and g-C_3N_4, which greatly improves the separation of electrons and holes in Ga_2O_3-DBD/g-C_3N_4. Moreover, the aromatic rings can also be used as electron mediators in Ga_2O_3-DBD/g-C_3N_4, improving its activity and stability. This research provides a novel approach for the fabrication of a Z-scheme photocatalytic system, which may serve as a universal method for the design of high-efficiency photocatalysts using other metal oxide and semiconductors.

2. Experimental

2.1. Materials

Hydrochloric acid, 3,4-dihydroxybenzaldehyde, Ga_2O_3, urea, methanol and tert butyl alcohol (TBA) were purchased from Aladdin Industrial Inc. All chemicals were analytical grade and used without further purification.

2.2. Preparation of aldehyde-functionalized Ga_2O_3 NPs

To modify the surface of Ga_2O_3 with aldehyde (–CHO), 3,4-dihydroxybenzaldehyde (DBD) was selected to react with Ga_2O_3 via metal–catechol complexation. Briefly, 0.5 g of Ga_2O_3 was added to 10 mL of a HCl solution (pH = 2) and stirred for 30 min. Then, a 50 mg/L 3,4-dihydroxybenzaldehyde solution (molar ratio of Ga_2O_3:DBD = 1:5) was slowly added to the mixture and stirred for another 2 h. The grey and wispy Ga_2O_3-DBD NPs were collected through centrifugation and washed several times with ethanol and water. Finally, the material was dried in the oven at 60 °C overnight.

2.3. Preparation of xGa_2O_3-DBD/g-C_3N_4

The xGa_2O_3-DBD/g-C_3N_4 photocatalysts were synthesized by direct thermal polymerization of Ga_2O_3-DBD NPs and urea following a typical synthesis procedure. Specifically, 20 g of urea and a certain amount of the Ga_2O_3-DBD NPs were thoroughly mixed; the resultant mixture was then placed in a covered porcelain crucible and calcined to 550 °C with a heating rate of 5 °C/min and kept at 550 °C for 2 h. After cooling down to room temperature, the samples were collected by centrifugation, washed with distilled water and dried in the oven at 60 °C overnight. The obtained samples were denoted as xGa_2O_3-DBD/g-C_3N_4, where x refers to the weight percentage of Ga_2O_3 calculated from the result of ICP.

2.4. Visible-light photocatalytic nitrogen fixation

Visible-light nitrogen photofixation experiments were performed in a quartz tube in a XPA-7 photochemical reactor. Briefly, 0.02 g of the photocatalyst was suspended in 50 mL of aqueous solution containing 0.04 mM methanol as a hole scavenger. Then, the mixture was continuously stirred in the dark for 30 min to obtain a uniform dispersion. Irradiation with a 500-W Xe lamp was then performed, and air or N_2 was bubbled at 100 mL/min through the solution. At given irradiation time intervals, 5 mL of the suspension was withdrawn and collected by centrifugation. The concentration of ammonia was measured using the Nessler's reagent spectrophotometry method (JB7478-87) with a UV-2550 spectrophotometer. The nitrogen fixation rate was calculated according to the following equation:

$$y = \frac{\Delta C}{18 \times \Delta t} \times 1000$$

where y ($\mu mol\ L^{-1}\ h^{-1}$) is the nitrogen fixation rate, C (mg/L) is the concentration of NH_4^+ at the time t.

2.5. Photocatalytic methylene blue (MB) degradation tests

The photocatalytic activities of the photocatalysts were tested by degradation of MB under visible light irradiation using a 500 W Xenon lamp. Briefly, 0.02 g of photocatalyst was added into 50 mL MB solution (20 mg L^{-1}). The mixture solution was stirring for 0.5 h in the dark to reach the adsorption-desorption equilibrium before turning on the Xenon lamp. 1 mL of suspension was withdrawn at every 30 min intervals and then filtered to remove photocatalyst particles. After reaction for 3 h, the concentration of MB was detected by the UV–vis spectrophotometer at the wavelength of 664 nm.

2.6. Detection of H_2O_2

The H_2O_2 content was measured using a fluorescence reagent (potassium hydrogen phthalate: 8.2 g/L, *p*-hydroxyphenylacetic acid: 270 mg/L and type-II horseradish peroxidase: 30 mg/L). Typically, 0.05 g of the photocatalyst was added into 50 mL of aqueous solution and irradiated using a 500-W Xe lamp. At 20-min intervals, 2 mL of the suspension was withdrawn and filtered to remove any photocatalyst particles. Then, 50 μL of the fluorescence reagent was added to the clear solution. After 10 min of reaction, 1 mL of 0.1 M NaOH solution was added. The concentration of H_2O_2 was measured using the UV-2550 spectrophotometer at 409 nm with excitation at 315 nm.

2.7. Characterization

X-ray diffraction (XRD) patterns were obtained using a Bruker D8 Advance diffractometer with Cu Kα radiation. Transmission electron microscopy (TEM) images were obtained using a JEOL JEM2100 microscope at an acceleration voltage of 200 kV. X-ray photoelectron spectroscopy (XPS) and valence band X-ray photoelectron spectroscopy (VBXPS) spectra were obtained using a PHI-5000 VersaProbe System with Al Kα radiation. Fourier-transform infrared (FT-IR) spectroscopy experiments were performed on a Nicolet IS 10 spectrometer. The temperature-programmed desorption of CO_2 (CO_2-TPD) was performed on a TP-5080 multi-functional automatic adsorption instrument. The zeta potentials of the samples in water were measured using

a Zetasizer nano ZS90 analyser. The distribution of the elements (C, N, O and Ga) in the sample was determined using a Titan G2 60-300 field-emission scanning electron microscope. The C, N, O and H contents were measured using a CHN-O-Rapid, and the Ga content in the xGa_2O_3-DBD/g-C_3N_4 was determined using inductively coupled plasma (ICP) with Optima 5300DV. The Brunauer–Emmett–Teller surface area was analysed by N_2 adsorption–desorption on a Micromeritics TriStarII 3020. The UV–visible (UV–vis) absorption spectra were obtained on a Hitachi U-3010 UV–vis spectrometer with $BaSO_4$ as a reference. Time-resolved fluorescence decay spectra were obtained on an Edinburgh FLSP920 spectrophotometer at an excitation wavelength of 340 nm. Photoluminescence (PL) spectra were measured using a Jobin Yvon SPEX Fluorolog-3-P spectroscope. The photocurrent was determined using a CHI 660B electrochemical workstation in a standard three-electrode system (Ag/AgCl (saturated NaCl) as the reference electrode). Electron paramagnetic resonance (EPR) spectra were obtained on a JEOL JES-FA200 spectrometer.

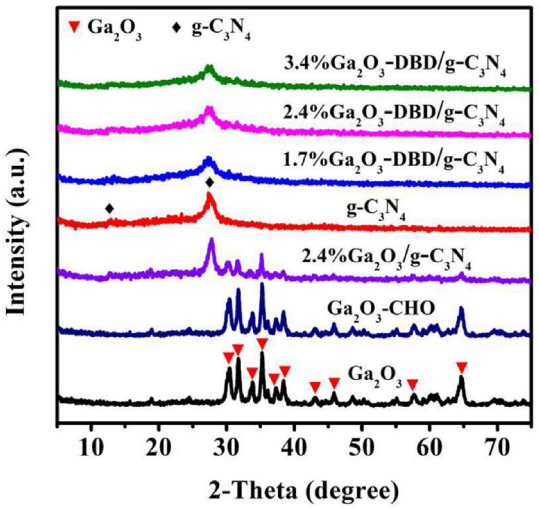

Fig. 1. XRD patterns of g-C_3N_4, Ga_2O_3, Ga_2O_3-CHO NPs and xGa_2O_3-DBD/g-C_3N_4.

3. Results and discussion

3.1. Result of characterization

A general scheme for the synthesis of xGa_2O_3-DBD/g-C_3N_4 is presented in Scheme 1. 3,4-dihydroxybenzaldehyde (DBD) is capable of strong interactions with metal oxides, which can react with Ga—OH, resulting in the dehydration and the formation of a charge-transfer complex [32,33]. The obtained mixture was Ga_2O_3-DBD NPs. The post-grafting incorporation of Ga_2O_3-DBD NPs into the carbon nitride networks was using a Schiff base chemistry reaction accompanied by the thermal polymerization of urea via an interaction of aromatic aldehydes and the terminal —NH_2 groups at the edge of the s-triazine ring [34–37]. Finally, the xGa_2O_3-DBD/g-C_3N_4 photocatalysts were obtained.

The C, N and O contents in g-C_3N_4 and xGa_2O_3-DBD/g-C_3N_4 were measured by elemental analysis, and the Ga content was determined using ICP. The results of the elemental analysis of g-C_3N_4 and xGa_2O_3-DBD/g-C_3N_4 are presented in Table 1. As expected, the atomic ratio of C to N gradually increased with increasing incorporation of Ga_2O_3-DBD NPs, which was caused by the incorporation of aromatics in the g-C_3N_4 networks. Notably, the H content of xGa_2O_3-DBD/g-C_3N_4 gradually decreased from 1.9 to 0.7 wt.% as the content of Ga_2O_3-DBD NPs increased from 1.7% to 4.3%, most likely because of the Schiff base chemistry reaction.

The structure of xGa_2O_3-DBD/g-C_3N_4 was characterized using XRD and compared with those of g-C_3N_4, Ga_2O_3 and Ga_2O_3-DBD NPs. The diffraction peaks in the pattern of Ga_2O_3 can be indexed to the monoclinic structure of β-Ga_2O_3 (JCPDS No. 43-1012) in Ga_2O_3 and Ga_2O_3-DBD NPs [38]. As observed in Fig. 1, the g-C_3N_4 phase was detected in the XRD spectra of xGa_2O_3-DBD/g-C_3N_4, whereas no diffraction of Ga_2O_3 was observed because the Ga_2O_3-DBD particles were well distributed on the surface of g-C_3N_4. The strong peak at approximately 27.4° indexed as (002) represented the interlayer stacking of aromatic systems. The other weak characteristic peak at 13.1° was indexed as (100) and represented an in-plane structural packing motif [39]. Notably, compared with the XRD patterns of g-C_3N_4, the overall diffraction intensities of xGa_2O_3-DBD/g-C_3N_4 were weak, indicating that grafting Ga_2O_3-DBD NPs could decrease the planar size of the layers of g-C_3N_4. For comparison, Ga_2O_3-DBD NPs were replaced by Ga_2O_3 NPs to prepare 2.4%Ga_2O_3/g-C_3N_4 under the same preparation conditions of 2.4%Ga_2O_3-DBD/g-C_3N_4. Compared with 2.4%Ga_2O_3-DBD/g-C_3N_4, diffraction peaks of Ga_2O_3 were observed for 2.4%Ga_2O_3/g-C_3N_4 (Fig. 1), which might be attributed to Ga_2O_3 particle agglomeration.

Porous structures were observed in the TEM images of xGa_2O_3-DBD/g-C_3N_4 (Fig. 2a–d), whereas an interlayer-like structure was observed in bulk g-C_3N_4 (Fig. S1). The pore structures of xGa_2O_3-DBD/g-C_3N_4 might be attributed to the steam generated through the reaction of aromatic aldehydes and the terminal —NH_2 groups during the calcination process. Moreover, the xGa_2O_3-DBD/g-C_3N_4 photocatalysts were thinned and fragmentized with increasing Ga_2O_3-DBD NPs content. The energy-dispersive X-ray spectroscopy spectra of the scanned area from Fig. 2b indicated that the hybrid was mainly composed of C, N, O and Ga; the elemental maps further illustrated that the Ga_2O_3-DBD NPs were successfully grafted onto the molecular structure of g-C_3N_4 (Fig. 2e). The morphologies of 2.4%Ga_2O_3-DBD/g-C_3N_4 and 2.4%Ga_2O_3/g-C_3N_4 were further investigated, and the results are compared in Fig. S2. Notably, the morphologies of the two samples differed. In detail, 2.4%Ga_2O_3/g-C_3N_4 exhibited a thick and interlayer-like structure (Fig. S2a), and most Ga_2O_3 particles were agglomerated without coating by g-C_3N_4, whereas a porous structure was observed and the Ga_2O_3-DBD NPs were well distributed on the surface for 2.4%Ga_2O_3-DBD/g-C_3N_4 (Fig. S2b). These findings were in good agreement with the XRD results, indicating that Ga_2O_3-DBD NPs could be well distributed on g-C_3N_4 networks via —CHO and —NH_2 interactions.

The elemental valence states of g-C_3N_4 and 2.4%Ga_2O_3-DBD/g-C_3N_4 were investigated by XPS. As observed in Fig. 3a, the C 1s signals of the pristine g-C_3N_4 could be deconvoluted into three peaks centred at 293.6, 288.0 and 284.6 eV, which corresponded to π-excitation, sp^2-bonded carbon (N=C—N) and the aromatic carbon atoms, respectively [40]. In contrast, 2.4%Ga_2O_3-DBD/g-C_3N_4 had a new C ls peak at 285.6 eV, which could be attributed to the phenolic hydroxyl groups. Notably, the peak at 284.6 eV in 2.4%Ga_2O_3-DBD/g-C_3N_4 was much stronger than that of g-C_3N_4, which was attributed to the incorporation of aromatic rings, further suggesting that the Ga_2O_3-DBD NPs have been successfully introduced into the g-C_3N_4 [41]. High-resolution N 1s spectra are presented in Fig. 3b. The N 1s spectrum contains four peaks centred at approximately 404.2, 400.8, 399.4 and 398.4 eV, which corresponded to π-excitation, amino functional groups (C—N—H), tertiary nitrogen groups (N—C_3) and the sp^2-hybridized nitrogen in s-triazine rings (C—N=C), respectively [42]. The content of amino functional groups (C—N—H) in 2.4%Ga_2O_3-DBD/g-C_3N_4 was lower than that of g-C_3N_4 (Table 1S). This result was consistent with the C 1s results. It indicated the reaction mechanism that the —NH_3 was most likely to transform into C=N via a Schiff base reaction between —NH_2 and —CHO groups, as illustrated in Scheme 1.

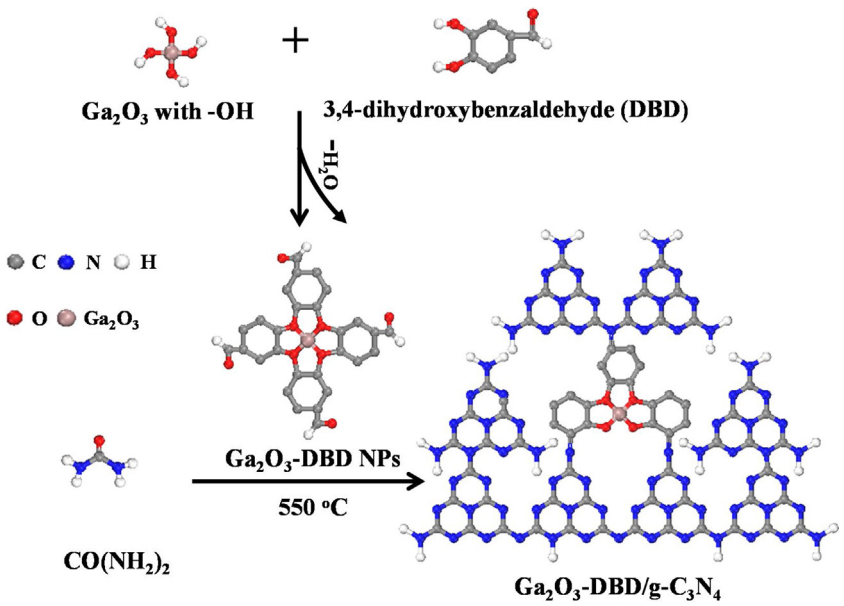

Scheme 1. The formation mechanism of xGa_2O_3-DBD/g-C_3N_4 photocatalyst.

Table 1
Elemental contents, BET surface areas, and band gaps of g-C_3N_4 and xGa_2O_3-DBD/g-C_3N_4.

Photocatalyst	Element content (wt%)					C/N atomic ratio	BET surface area ($m^2\ g^{-1}$)	Band gap (eV)
	C	N	H	O	Ga			
g-C_3N_4	32.9	58.4	1.9	6.7	–	0.657	61.3	2.67
1.7%Ga_2O_3-DBD/g-C_3N_4	32.8	57.7	1.9	6.9	1.3	0.662	66.2	2.65
2.4%Ga_2O_3-DBD/g-C_3N_4	34.0	54.5	1.6	8.7	1.8	0.723	72.4	2.63
3.4%Ga_2O_3-DBD/g-C_3N_4	34.6	53.3	1.1	10	2.5	0.757	84.5	2.60
4.3%Ga_2O_3-DBD/g-C_3N_4	34.4	50.6	0.7	12	3.2	0.793	78.6	2.56

Moreover, the binding energies of the O 1s peak are depicted in Fig. 3c. The peak centred at approximately 531.6 eV was attributed to the presence of loosely bound oxygen on the surface of g-C_3N_4, e.g. CO_2, adsorbed H_2O, or adsorbed O_2 [43]. A new peak at 530.4 eV appeared in 2.4%Ga_2O_3-DBD/g-C_3N_4, which was attributed to O^{2-} ions on the monoclinic structure of the Ga^{2+} ion array [44].

The chemical structures of g-C_3N_4 and xGa_2O_3-DBD/g-C_3N_4 were further characterized using FTIR spectroscopy. As observed in Fig. 4a, xGa_2O_3-DBD/g-C_3N_4 was characterized by typical IR patterns of g-C_3N_4, indicating that the main chemical skeleton of g-C_3N_4 has been retained, which was consistent with the XRD results. The intense peak at 815 cm^{-1} corresponded to the breathing mode of the heptazine units, and the multiple bands at 1200–1600 cm^{-1} were attributed to the stretching vibration modes of tri-s-triazine heterocyclic stretches. In addition, the broad band between 3185 and 3261 cm^{-1} was mainly associated with the stretching mode of N—H [42,45]. Surprisingly, the absorption band of N—H for xGa_2O_3-DBD/g-C_3N_4 was weakened compared with that of g-C_3N_4, which might be explained by several C—NH groups having been replaced by C═N groups after post-grafting modification of Ga_2O_3-DBD NPs. Moreover, compared with the 2.4%Ga_2O_3-DBD/g-C_3N_4, there are more new IR bands in physically-mixed power of Ga_2O_3-DBD and g-C_3N_4, and the absorption band of N—H was also stronger, which indicated that there were no chemical interaction between Ga_2O_3-DBD and g-C_3N_4 and the C—NH groups were not be replaced in physically-mixed samples (Fig. S3). The difference of FTIR spectrum further confirmed that Ga_2O_3-DBD and g-C_3N_4 were interrelated and interacted with each other by chemical bond in 2.4%Ga_2O_3-DBD/g-C_3N_4 while physically-mixed power of Ga_2O_3-DBD and g-C_3N_4 had no chemical interaction. In addition, g-C_3N_4, 2.4%Ga_2O_3/g-C_3N_4 and 2.4%Ga_2O_3-DBD/g-C_3N_4 were further characterized by high-resolution FT-IR spectroscopy. As presented in Fig. 4b, 2.4%Ga_2O_3-DBD/g-C_3N_4 exhibited new weak IR bands at approximately 1500 cm^{-1}. The bands in this range were primarily caused by aromatics, further confirming that aromatic rings were successfully grafted onto the g-C_3N_4 networks [34,42].

To prove the post-grafting incorporation mechanism of Ga_2O_3-DBD NPs into the g-C_3N_4 networks based on the Schiff base chemistry, the variation of the —NH_2 groups was investigated using CO_2-TPD and zeta potential measurements of g-C_3N_4, 2.4%Ga_2O_3/g-C_3N_4 and 2.4%Ga_2O_3-DBD/g-C_3N_4. As shown in Fig. 4c, all the samples exhibited a broad peak centred at 185 °C, which was attributed to the strong interaction of the basic groups (originating from the free —NH_2 groups in g-C_3N_4) with slightly acidic CO_2 molecules [46]. Compared with g-C_3N_4, the lower CO_2 desorption peak of 2.4%Ga_2O_3/g-C_3N_4 could be attributed to the hydroxyl group of Ga_2O_3, which could interact with the surface —NH_2 groups on g-C_3N_4. Among the three samples, 2.4%Ga_2O_3-DBD/g-C_3N_4 had the lowest CO_2 desorption peak, indicating that the —NH_2 content was further decreased after the incorporation of Ga_2O_3-DBD NPs via the interaction of —NH_2 and —CHO groups. In addition, —NH_2 groups could act as proton acceptors and acquire positive surface charges [46]. Fig. 4d revealed that the zeta potential of 2.4%Ga_2O_3-DBD/g-C_3N_4 (−38.2 mV) was more negative than those of g-C_3N_4 (−20.4 mV) and 2.4%Ga_2O_3/g-C_3N_4 (−25.6 mV). These findings confirmed that the content of terminal —NH_2 groups in 2.4%Ga_2O_3-DBD/g-C_3N_4 significantly decreased. Based on these analyses, it could be concluded that the aromatic rings were successfully grafted onto the molecular structure of g-C_3N_4 in xGa_2O_3-DBD/g-C_3N_4 by the reaction of aromatic aldehydes and the terminal —NH_2 groups, which was beneficial for the dispersion of Ga_2O_3-DBD NPs on the g-C_3N_4 networks and the formation

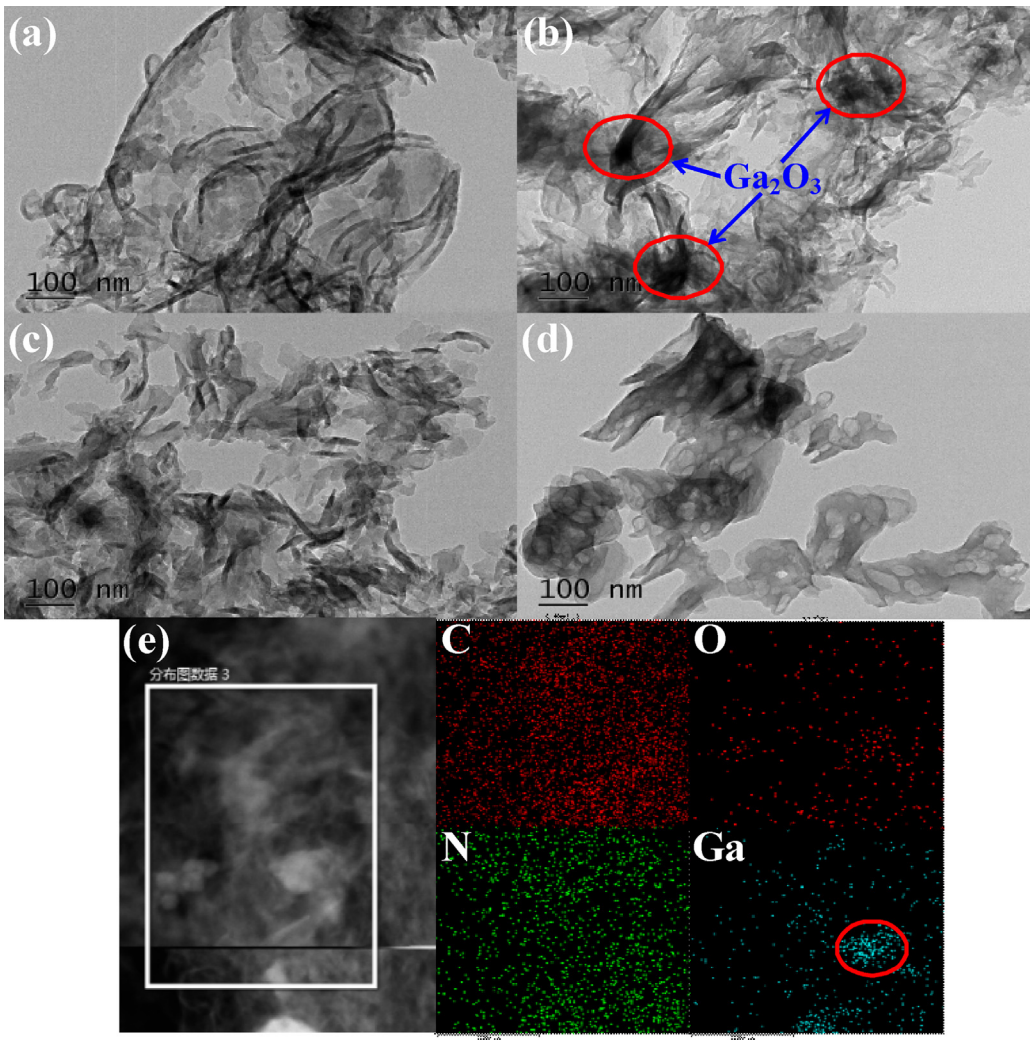

Fig. 2. TEM images of (a) 1.7%Ga_2O_3-DBD/g-C_3N_4, (b) 2.4%Ga_2O_3-DBD/g-C_3N_4, (c) 3.4%Ga_2O_3-DBD/g-C_3N_4 and (d) 4.3%Ga_2O_3-DBD/g-C_3N_4, and (e) the TEM-EDX mapping of 2.4%Ga_2O_3-DBD/g-C_3N_4.

of a well-developed combined interface between Ga_2O_3-DBD and g-C_3N_4.

3.2. Visible light photocatalytic nitrogen photofixation

3.2.1. Photocatalytic performance of xGa_2O_3-DBD/g-C_3N_4

The photocatalytic nitrogen fixation activities of g-C_3N_4 and xGa_2O_3-DBD/g-C_3N_4 are presented in Fig. 5a. Clearly, xGa_2O_3-DBD/g-C_3N_4 exhibited superior photocatalytic activities compared with that of g-C_3N_4. Among the xGa_2O_3-DBD/g-C_3N_4 photocatalysts, 2.4%Ga_2O_3-DBD/g-C_3N_4 presented the best photocatalytic activity with a nitrogen fixation rate of 112.5 μmol L^{-1} h^{-1}, which was 3.37 times higher than that of bulk g-C_3N_4 (33.4 μmol L^{-1} h^{-1}). However, the nitrogen fixation rate decreased with further increasing of the Ga_2O_3-DBD content, which might be attributed to the over-fragmentization of the g-C_3N_4 structure leading to easier dissipation of photo-generated charge carriers into vibrational or thermal energy.

The UV–vis diffuse reflectance spectroscopy (DRS) spectra of g-C_3N_4 and xGa_2O_3-DBD/g-C_3N_4 are compared in Fig. 5b to illuminate the intrinsic electronic/optical properties of the photocatalysts. With the increase in the amount of Ga_2O_3-DBD NPs, the xGa_2O_3-DBD/g-C_3N_4 photocatalysts showed an improvement of the light absorption in both the UV and visible regions compared with g-C_3N_4. This phenomenon was attributed to the visible-light response of g-C_3N_4 and the UV-light response of Ga_2O_3. This result might be attributed to two phenomena: the extended 2D electron delocalization, caused by aromatic rings incorporation, and the activation of an n to p* electron transition because of the distorted structure of xGa_2O_3-DBD/g-C_3N_4 [47,48]. Moreover, with the increased amount of grafted Ga_2O_3-DBD NPs, intensified and red-shifted light absorption was observed (Fig. 5b), further verifying the previously presented analysis. The corresponding band gaps of xGa_2O_3-DBD/g-C_3N_4 decreased from 2.67 to 2.56 eV as the content of Ga_2O_3 increased from 1.7% to 4.3% (Fig. S4), as calculated using the Kubelka–Munk method, implying that the electronic structure of g-C_3N_4 has been modified by grafting of aromatic rings.

As observed in Fig. 5c, the lifetime of charge carriers decreased with increasing grafting of Ga_2O_3-DBD NPs, from 3.152 ns for pristine g-C_3N_4 to 2.763 ns for 4.3%Ga_2O_3-DBD/g-C_3N_4, which might be due to the efficient charge separation. It was reported that the decreased fluorescence lifetime indicated that the relaxation of a fraction of photocatlysts excited states occurs via nonradiative paths and was related to higher turnover frequency (TOF) of photocatalytic H_2 generation. Therefore, xGa_2O_3-DBD/g-C_3N_4 excited states via charge transfer of electrons and holes to new localized/surface states, which might facilitate charge generation and consequently enhance the photocatalytic activity [40,49]. The transfer and separation abilities of the carriers were determined via PL (Fig. 5d). The PL intensities of xGa_2O_3-DBD/g-C_3N_4

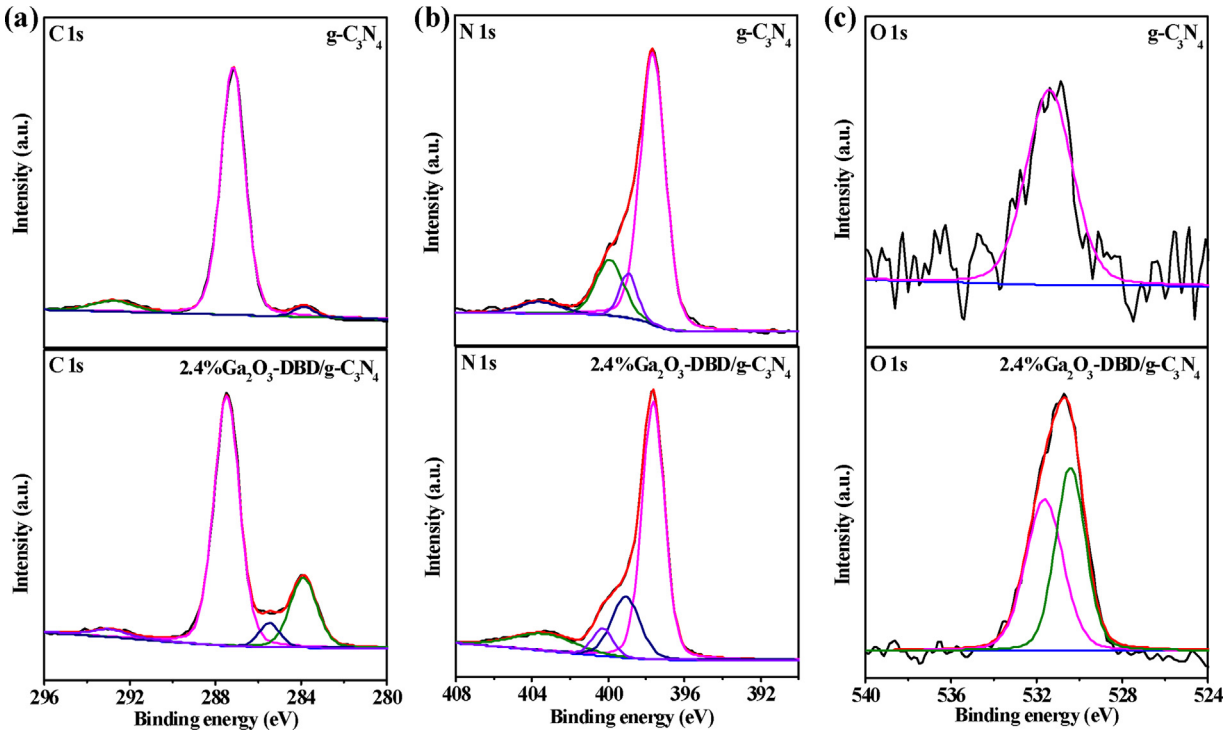

Fig. 3. The high resolution (a) C 1s, (b) N 1s, (c) O 1s XPS spectra of g-C_3N_4 and 2.4%Ga_2O_3-DBD/g-C_3N_4.

tremendously decreased upon the incorporation of Ga_2O_3-DBD NPs, indicating that the recombination of charge carriers was highly suppressed. The spatial separation of photogenerated charge carriers was improved in xGa_2O_3-DBD/g-C_3N_4 as compared to g-C_3N_4. This phenomena may be attributed to the following contributions: (1) the dissipation of terminal $-NH_2$, which served to decrease the charge carrier recombination rate, and (2) the introduction of an electron mediator (aromatic rings), which could enhance the charge transfer transition. In conclusion, the incorporation of Ga_2O_3-DBD NPs enhanced the light-harvesting capability and increased the charge density and mobility, significantly improving photocatalytic activity.

To evaluate the stability of 2.4%Ga_2O_3-DBD/g-C_3N_4, a four-cycle recycling experiment was performed. As shown in Fig. 5e, the nitrogen fixation rate exhibited a slight decrease during the cycling rounds, which might be attributed to the loss of photocatalyst particles during the recycling runs and/or experimental error. To further identify the photostability of the 2.4%Ga_2O_3-DBD/g-C_3N_4, TEM, XRD and XPS and FT-IR analysis of samples before and after cycling experiments were further performed. As observed in Fig. S5, there was no notable difference in the spectra of 2.4%Ga_2O_3-DBD/g-C_3N_4 after recycling for four times, suggesting excellent chemical and photochemical stabilities.

3.2.2. Nitrogen photofixation mechanism

To determine the produced reactive oxygen species (ROS) in nitrogen photofixation over 2.4%Ga_2O_3-DBD/g-C_3N_4, the 5,5-dimethyl-1-pyrroline-N-oxide (DMPO) spin-trapping EPR technique was employed. As shown in Fig. 6a, four characteristic peaks of DMPO/$^{\bullet}O_2^-$ were observed in 2.4%Ga_2O_3—C_3N_4, whereas only a trace level of the DMPO/$^{\bullet}O_2$ signal could be detected for 2.4%Ga_2O_3-DBD/g-C_3N_4 under the same conditions. However, the 2.4%Ga_2O_3-DBD/g-C_3N_4 system produced approximately 2.3 times more H_2O_2 than the 2.4%Ga_2O_3/g-C_3N_4 system (Fig. S6a). This finding indicates that the H_2O_2 generated by 2.4%Ga_2O_3/g-C_3N_4 was generated through direct reduction ($O_2 \rightarrow H_2O_2$) and not via a multistep reaction ($O_2 \rightarrow {}^{\bullet}O_2^- \rightarrow H_2O_2$) from oxygen, which could be attributed to the stronger oxidation ability of 2.4%Ga_2O_3-DBD/g-C_3N_4. Meanwhile, the relative concentration of $^{\bullet}OH$ was estimated and is shown in Fig. 6b. The characteristic peaks of DMPO/$^{\bullet}OH$ were observed in 2.4%Ga_2O_3-DBD/g-C_3N_4, and the intensity was much stronger than that of 2.4%Ga_2O_3/g-C_3N_4. The stronger intensity of $^{\bullet}OH$ in 2.4%Ga_2O_3-DBD/g-C_3N_4 might be resulted from the presence of more H_2O_2 ($H_2O_2 + e^- \rightarrow {}^{\bullet}OH + OH^-$) and direct oxidation of OH^- by holes ($h^+ + OH^- \rightarrow {}^{\bullet}OH$). To confirm this speculation, photocatalytic nitrogen fixation over 2.4%Ga_2O_3-DBD/g-C_3N_4 and 2.4%Ga_2O_3/g-C_3N_4 was investigated under different atmospheres. As observed in Fig. 6c, the photocatalytic N_2 fixation of 2.4%Ga_2O_3-DBD/g-C_3N_4 clearly decreased with the absence of O_2 because of the lack of $^{\bullet}OH$, which originated from the H_2O_2. It is worth noting that there was no N_2 fixation activity of 2.4%Ga_2O_3-DBD/g-C_3N_4 under Ar atmospheres, which ascribed to the absence of nitrogen source. This phenomenon suggested that the stability of 2.4%Ga_2O_3-DBD/g-C_3N_4 photocatalyst were excellent and had no influence on nitrogen fixation (Fig. S6b). The activity remained higher than that of 2.4%Ga_2O_3/g-C_3N_4 because of the extra $^{\bullet}OH$ that could form through the direct oxidation of OH^- by holes. The generated $^{\bullet}OH$ more easily reacted with methanol to form $^{\bullet}CO_2^-$ (Fig. 6d). The strong reducing ability of $^{\bullet}CO_2^-$ ($E_{CO_2/^{\bullet}CO_2^-} = 1.8$ V) can facilitate reduction of N_2 to NH_3 [50,51]. To further confirm the role of indirect electron transfer caused by $^{\bullet}CO_2^-$, the photocatalytic nitrogen fixation over 2.4%Ga_2O_3-DBD/g-C_3N_4 was further investigated by using tert butyl alcohol (TBA) as hole scavengers. Alcohols with lower E_{HOMO} (energy of the highest occupied molecular orbital) can be more easily oxidized, which plays a crucial role in the improvement of catalytic performance [10]. As a sacrificial reagent, methanol is more suitable and effective than TBA due to the lower HOMO. However, the photocatalytic N_2 fixation of 2.4%Ga_2O_3-DBD/g-C_3N_4 was further improved by TBA (Fig. S6c). This result was attributed to the increased formation rate of $^{\bullet}CO_2^-$, which led to the enhancement of the indirect electron transfer rate.

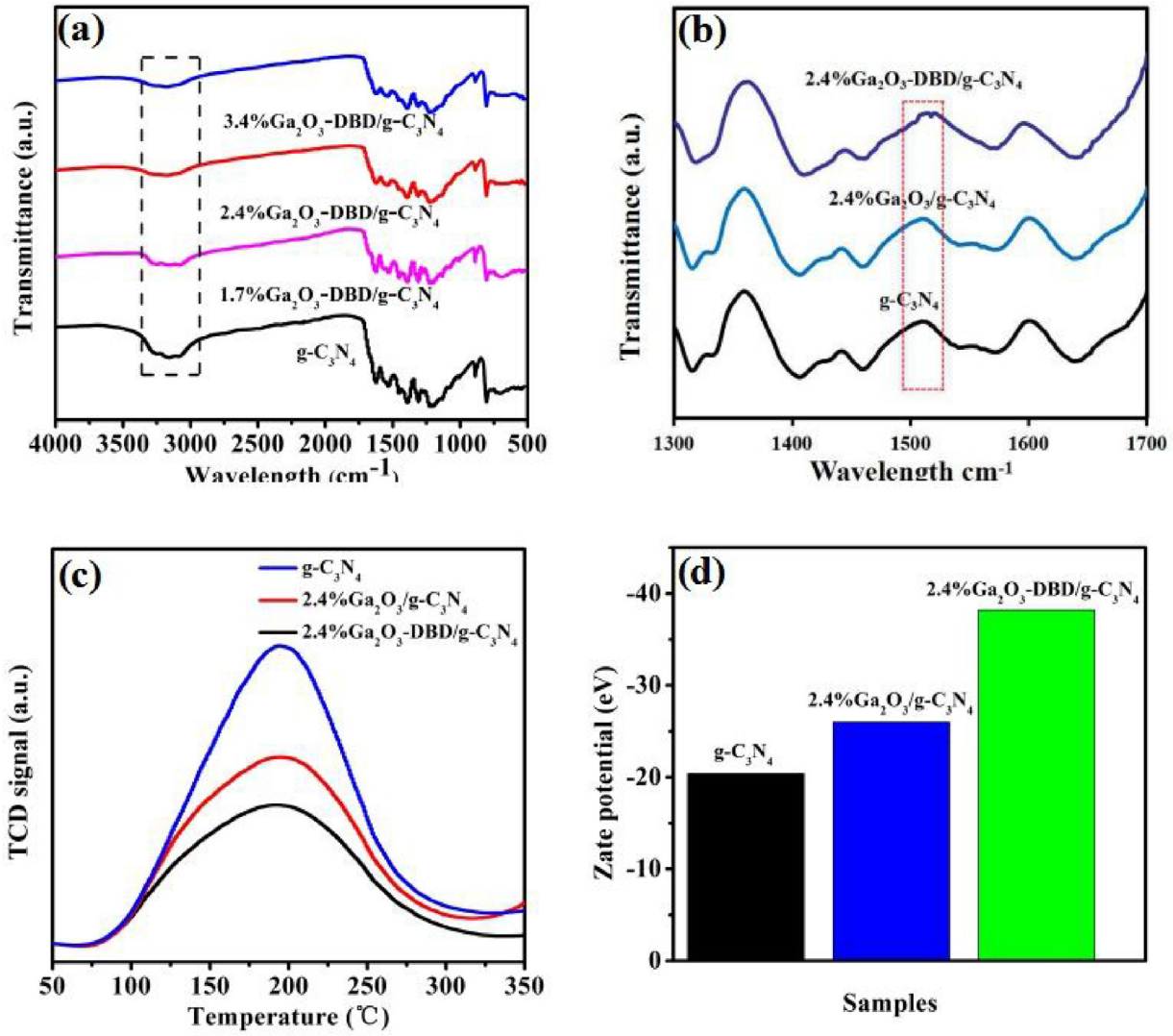

Fig. 4. (a) FTIR spectra of g-C_3N_4 and xGa_2O_3-DBD/g-C_3N_4. (b) High-resolution FTIR spectra, (c) CO_2 TPD profiles and (d) Zeta potentials of g-C_3N_4, 2.4%Ga_2O_3/g-C_3N_4 and 2.4%Ga_2O_3-DBD/g-C_3N_4.

As illustrated in Scheme 2, the photo-generated electron transfer between g-C_3N_4 and Ga_2O_3 can be classified into one of two models. The valence band edge of g-C_3N_4 and Ga_2O_3 was determined from comprehensive UV–vis DRS and VBXPS analyses (Fig. S7). The first model comprises donor–acceptor charge separation, as illustrated in Scheme 2a, in which photogenerated electron transfer occurs from the conduction band (CB) of g-C_3N_4 to that of Ga_2O_3 and hole transfer occurs from the valence band (VB) of Ga_2O_3 to that of g-C_3N_4, resulting in the weakened redox ability of photogenerated electrons and holes. If the charge migration of xGa_2O_3-DBD/g-C_3N_4 occurs via this model, H_2O_2 and •OH radicals cannot be produced because the CB potential of Ga_2O_3 (−0.67 eV vs. normal hydrogen electrode (NHE)) is more positive than E_0 (O_2/H_2O_2 = −0.695 eV vs. NHE) and the VB potential of g-C_3N_4 (+1.73 eV vs. NHE) is more negative than E_0 (•OH/OH^- = +1.99 eV vs. NHE) [40,52]. Therefore, a second model (Z-scheme charge migration) was proposed. As illustrated in Scheme 2b, the photogenerated electron transfer occurs from the CB of Ga_2O_3 to the VB of g-C_3N_4 via the aromatic rings, leaving an electron in the CB of g-C_3N_4 and a hole in the VB of Ga_2O_3. The CB potential of g-C_3N_4 (−0.94 eV vs. NHE) is more negative than E_0 (O_2/H_2O_2), and the VB potential of Ga_2O_3 (+3.45 eV vs. NHE) is more positive than E_0 (•OH/OH^-). That is, the electrons in the CB of g-C_3N_4 can direct reduce O_2 to H_2O_2 and the holes in the VB of Ga_2O_3 can react with H_2O to generate •OH, which is consistent with the EPR results.

To clarify the effect of aromatic rings on the photocatalysis, visible-light photocatalytic nitrogen fixation over 2.4%Ga_2O_3-DBD/g-C_3N_4 and 2.4%Ga_2O_3/g-C_3N_4 was investigated. As observed in Fig. 6c, the photocatalytic nitrogen fixation activity of 2.4%Ga_2O_3-DBD/g-C_3N_4 was better than that of 2.4%Ga_2O_3/g-C_3N_4. Similar improved ability of 2.4%Ga_2O_3-DBD/g-C_3N_4 was demonstrated through the photocatalytic degradation of MB under visible-light irradiation. In other words, the redox ability of 2.4%Ga_2O_3-DBD/g-C_3N_4 was stronger than that of 2.4%Ga_2O_3/g-C_3N_4 photocatalyst (Fig. S8). The UV–vis spectrum of 2.4% Ga_2O_3-C_3N_4 (Fig. 5b) displayed only extended-light response with no red-shift compared with that of g-C_3N_4, which could be attributed to the formation of the surface/interfacial heterojunctions between Ga_2O_3 and g-C_3N_4. However, the 2.4%Ga_2O_3-DBD/g-C_3N_4 catalysts demonstrated improvement of light absorption in both the UV and visible regions. Moreover, the PL emission peaks of 2.4%Ga_2O_3-C_3N_4 were much lower than those of 2.4%Ga_2O_3-DBD/g-C_3N_4 (Fig. 5d), indicating that these two photocatalysts follow different models of electron transfer between Ga_2O_3 and g-C_3N_4. Specifically, 2.4%Ga_2O_3-DBD/g-C_3N_4 was a Z-scheme photocatalytic system, in which electrons and holes could be quenched, whereas 2.4%Ga_2O_3-

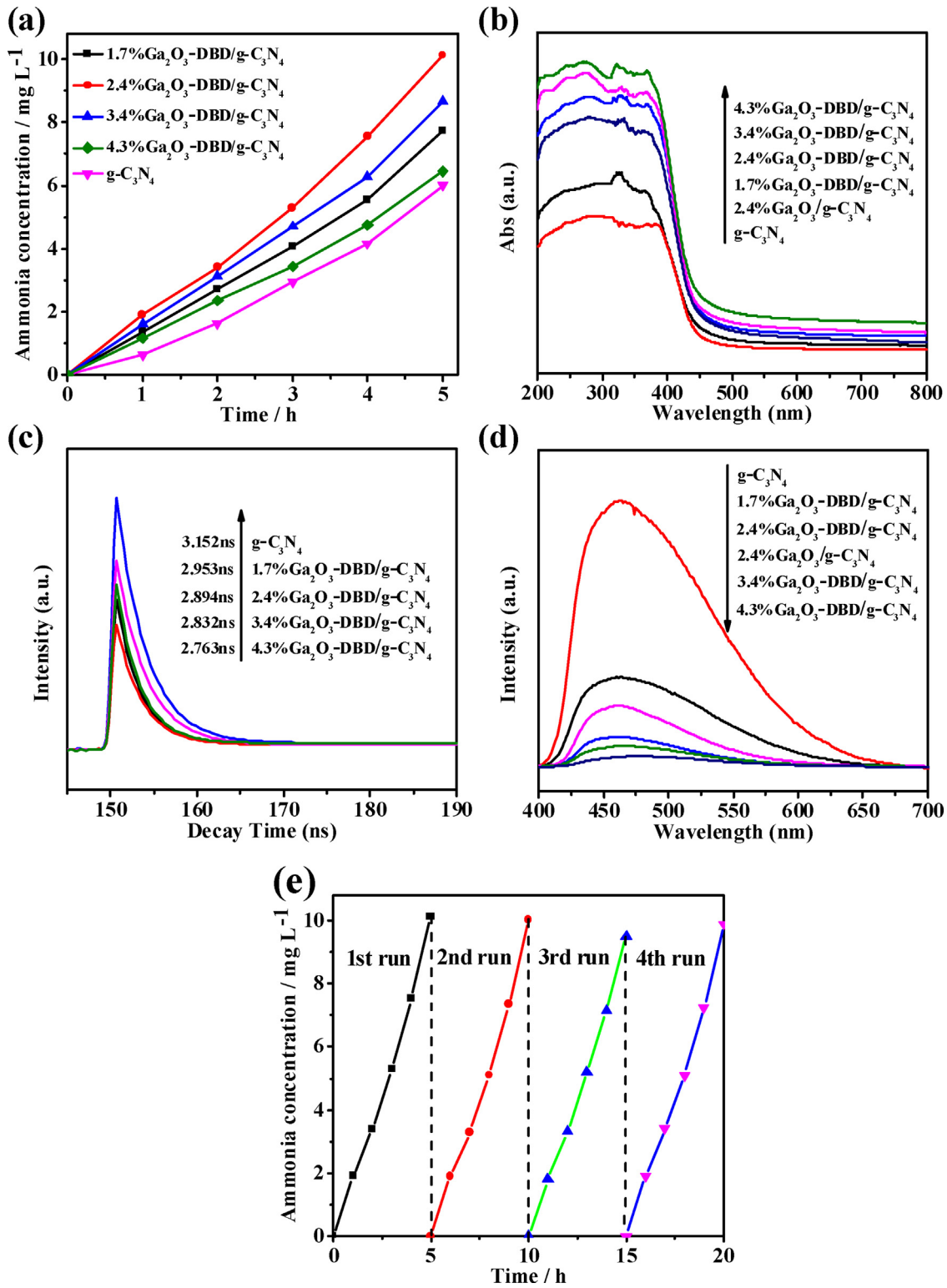

Fig. 5. (a) Visible light photocatalytic nitrogen fixation over g-C_3N_4 and xGa_2O_3-DBD/g-C_3N_4. (b) UV–vis diffuse reflectance spectra of g-C_3N_4, 2.4%Ga_2O_3/g-C_3N_4 and xGa_2O_3-DBD/g-C_3N_4. (c) Time-resolved PL spectra of g-C_3N_4 and xGa_2O_3-DBD/g-C_3N_4. (d) PL spectra of g-C_3N_4, 2.4%Ga_2O_3/g-C_3N_4 and xGa_2O_3-DBD/g-C_3N_4. (e) Cycling runs for the visible light nitrogen fixation over 2.4%Ga_2O_3-DBD/g-C_3N_4.

C_3N_4 was a heterojunction-type photocatalytic system, in which the recombination of charge carriers was inhibited. The photocurrent response curves are presented in Fig. 6e. The photocurrent of 2.4%Ga_2O_3-DBD/g-C_3N_4 was much higher than that of 2.4%Ga_2O_3-C_3N_4, indicating that the aromatic rings could efficiently promote the separation and transfer of photogenerated charge carriers. The consistent conclusion was also supported by electrochemical impedance spectroscopy measurements (Fig. 6f), which revealed an obvious decrease in the semicircular Nyquist plots for 2.4%Ga_2O_3-DBD/g-C_3N_4 over 2.4%Ga_2O_3-C_3N_4. Based on this analysis, it was clear that the aromatic rings were beneficial for the absorption of visible light, promotion of the separation and transfer of pho-

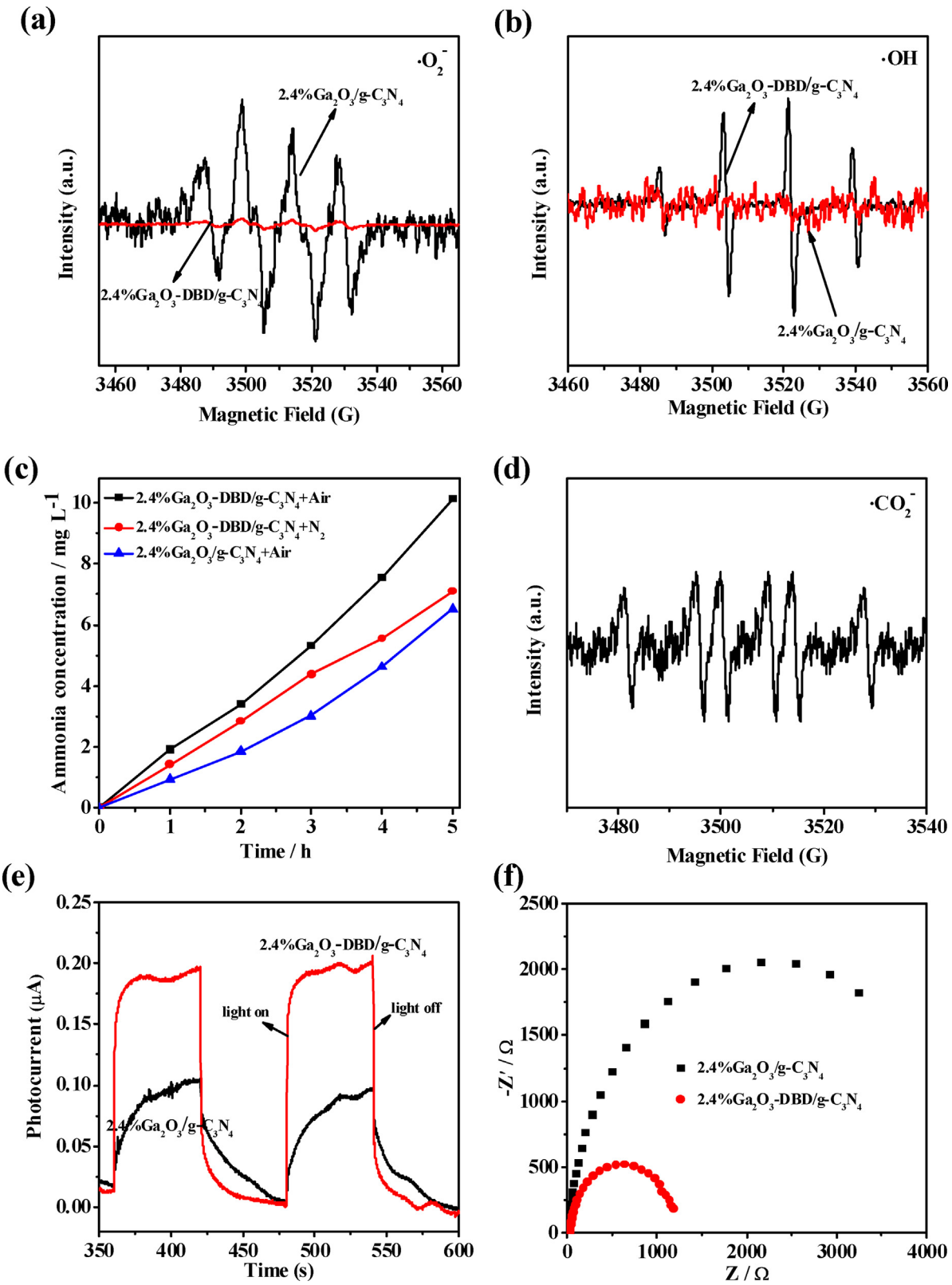

Fig. 6. DMPO spin-trapping ESR spectra recorded for (a) $^{\bullet}O^{2-}$ and (b) $^{\bullet}OH$ in 2.4%Ga_2O_3/g-C_3N_4 and 2.4%Ga_2O_3-DBD/g-C_3N_4. (c) Visible light nitrogen fixation over 2.4%Ga_2O_3/g-C_3N_4 and 2.4%Ga_2O_3-DBD/g-C_3N_4 under different atmospheres. (d) DMPO spin-trapping ESR spectra recorded for $^{\bullet}CO_2^-$ in 0.2 mol L^{-1} methanol aqueous solution. (e) Photocurrent transient responses and (f) electrochemical impedance spectroscopy (EIS) Nyquist plots in the dark of 2.4%Ga_2O_3/g-C_3N_4 and 2.4%Ga_2O_3-DBD/g-C_3N_4.

togenerated charge carriers, as well as the change of the model of electron transfer between Ga_2O_3 and g-C_3N_4, resulting in the successful construction of the Z-scheme systems.

Based on these comparative investigations, a detailed photocatalysis mechanism and the role of aromatic rings in the Z-scheme type Ga_2O_3-DBD/g-C_3N_4 system are proposed and illustrated in

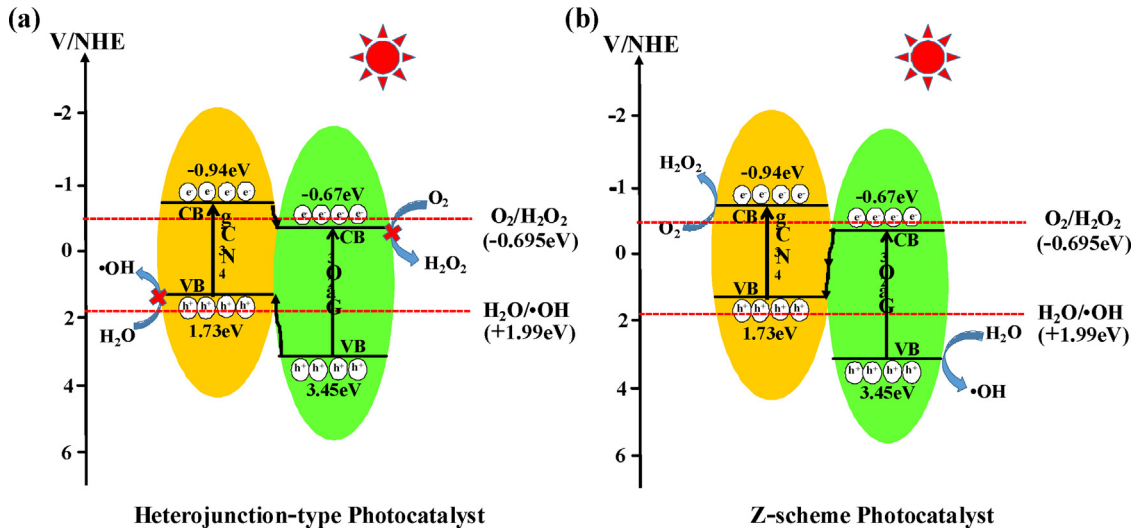

Scheme 2. The schematic illustration of two possible photocatalytic systems of xGa_2O_3-DBD/g-C_3N_4: (a) heterojunction-type and (b) Z-scheme photocatalytic system.

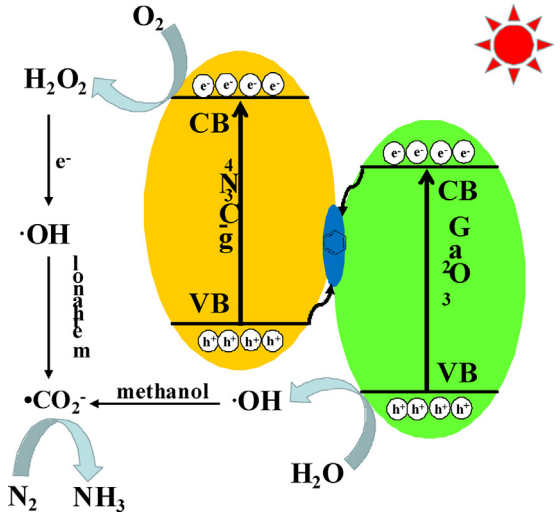

Scheme 3. Photocatalytic nitrogen fixation mechanism over Z-scheme xGa_2O_3-DBD/g-C_3N_4.

Scheme 3. During the reaction of nitrogen photofixation, photo-generated electrons in the CB of g-C_3N_4 could directly reduce O_2 to H_2O_2, and the holes in the VB of Ga_2O_3 might be involved in the production of $^{\bullet}OH$ from H_2O. The methanol was then oxidized to $^{\bullet}CO_2^-$ by these active oxygen species, facilitating the reduction of N_2 to NH_3. The possible photocatalytic reaction processes were listed as follows:

$$Ga_2O_3\text{-DBD/g-}C_3N_4 + \text{visible light} \rightarrow e^- + h^+$$

$$2O_2 + 2e^- + 4H_2O \rightarrow 3H_2O_2 + 2OH^-$$

$$H_2O_2 + e^- \rightarrow {}^{\bullet}OH + OH^-$$

$$h^+ + OH^- \rightarrow {}^{\bullet}OH$$

$$^{\bullet}OH + \text{methanol} \rightarrow {}^{\bullet}CO_2^- + \text{intermediates}$$

$$N_2 + 2{}^{\bullet}CO_2^- + 4H_2O \rightarrow 2NH_3 + 2CO_2 + 2OH^-$$

4. Conclusion

A novel post-grafting strategy based on Schiff base chemistry was developed to construct an all-solid-state Z-scheme Ga_2O_3-DBD/g-C_3N_4 heterojunction. The interaction between aromatic aldehydes in Ga_2O_3-DBD and the terminal $-NH_2$ groups in g-C_3N_4 promoted the dispersion of Ga_2O_3-DBD NPs and led to the formation of a well-developed combined interface, which greatly promoted the transfer of charge carriers. The photocatalytic nitrogen fixation rate of 2.4%Ga_2O_3-DBD/g-C_3N_4 (112.5 $\mu mol\ L^{-1}\ h^{-1}$) was 3.37 times faster that of g-C_3N_4 (33.4 $\mu mol\ L^{-1}\ h^{-1}$). An investigation of the photocatalysis mechanism suggested that aromatic rings with excellent conductivity could act as electron mediators; the photo-generated electrons transfered from the CB of Ga_2O_3 to the VB of g-C_3N_4 via the aromatic rings, leaving an electron in the CB of g-C_3N_4 and a hole in the VB of Ga_2O_3, thus enhancing the redox ability of the charge carriers; the hole can directly oxidize OH^- to $^{\bullet}OH$, whereas the electron could directly reduce O_2 to H_2O_2. Moreover, methanol was oxidized to $^{\bullet}CO_2^-$ by active oxygen species, facilitating N_2 reduction to NH_3. This study provides a new insight into the design of a Z-scheme Ga_2O_3-DBD/g-C_3N_4 heterojunction via non-metal materials (aromatic rings), which has great potential for solving the energy and environmental crises.

Acknowledgements

The financial supports from the Natural Science Foundation of China (Nos. 51678306 and 51478223) and the Natural Science Foundation of Jiangsu Province (BK2012405), China Postdoctoral Science Foundation (2013M541677, 2016M590458), the Jiangsu Planned Projects for Postdoctoral Research Funds (1202007B), the Fundamental Research Funds for the Central University (30915011308) are gratefully acknowledged.

Appendix A. Supplementary data

Supplementary data associated with this article can be found, in the online version, at http://dx.doi.org/10.1016/j.apcatb.2017.07.013.

References

[1] S. Sun, X. Li, W. Wang, L. Zhang, X. Sun, Appl. Catal. B: Environ. 200 (2017) 323–329.

[2] J. Li, H. Li, G.M. Zhan, L.Z. Zhang, Acc. Chem. Res. 50 (2017) 112–121.
[3] P.C. Dos Santos, R.Y. Igarashi, H. Lee, B.M. Hoffman, L.C. Seefeldt, D.R. Dean, Acc. Chem. Res. 38 (2005) 208–214.
[4] A. Banerjee, B.D. Yuhas, E.A. Margulies, Y. Zhang, Y. Shim, M.R. Wasielewski, M.G. Kanatzidis, J. Am. Chem. Soc. 137 (2015) 2030–2034.
[5] T. Oshikiri, K. Ueno, H. Misawa, Angew. Chem. Int. Ed. 53 (2014) 9802–9805.
[6] H. Li, J. Shang, J. Shi, K. Zhao, L. Zhang, Nanoscale 8 (2016) 1986–1993.
[7] A.J. Medford, M.C. Hatzell, ACS Catal. 7 (2017) 2624–2643.
[8] H. Li, J. Shang, Z. Ai, L. Zhang, J. Am. Chem. Soc. 137 (2015) 6393–6399.
[9] E. Endoh, J.K. Leland, A.J. Bard, J. Phys. Chem. 90 (1986) 6223–6226.
[10] W. Zhao, H. Xi, M. Zhang, Y. Li, J. Chen, J. Zhang, X. Zhu, Chem. Commun. 51 (2015) 4785–4788.
[11] G. Wu, Y. Gao, B. Zheng, Ceram. Int. 42 (2016) 6985–6992.
[12] J. Ding, Z. Dai, F. Qin, H. Zhao, S. Zhao, R. Chen, Appl. Catal. B: Environ. 205 (2017) 281–291.
[13] L. Ye, C. Han, Z. Ma, Y. Leng, J. Li, X. Ji, D. Bi, H. Xie, Z. Huang, Chem. Eng. J. 307 (2017) 311–318.
[14] I. Hwang, M. Baek, K. Yong, ACS Appl. Mater. Interfaces 7 (2015) 27863–27870.
[15] X. Jia, J. Cao, H. Lin, M. Zhang, X. Guo, S. Chen, Appl. Catal. B: Environ. 204 (2017) 505–514.
[16] H. Fan, D. Wang, T. Xie, Y. Liu, Chem. Phys. Lett. 640 (2015) 188–193.
[17] R. Hou, Y. Gao, H. Zhu, G. Yang, W. Liu, Y. Huo, Z. Xie, H. Li, Chem. Eng. J. 317 (2017) 386–393.
[18] X. Huang, Y. Xia, Y. Cao, X. Zheng, H. Pan, J. Zhu, C. Ma, H. Wang, J. Li, R. You, S. Wei, W. Huang, J. Lu, Nano Res. 10 (2017) 1302–1312.
[19] Q. Li, N. Zhang, Y. Yang, G. Wang, D.H. Ng, Langmuir 30 (2014) 8965–8972.
[20] J. Qin, M. Cao, N. Li, C. Hu, J. Mater. Chem. 21 (2011) 17167–17174.
[21] J. Sun, X. Li, Q. Zhao, J. Ke, D. Zhang, J. Phys. Chem. C 118 (2014) 10113–10121.
[22] H. Chen, S. Cao, J. Yao, F. Jiang, J. Taiwan Inst. Chem. Eng. 71 (2017) 189–196.
[23] C. Jia, P. Yang, B. Huang, ChemCatChem 6 (2014) 611–617.
[24] P. Zhou, J. Yu, M. Jaroniec, Adv. Mater. 26 (2014) 4920–4935.
[25] B. Liu, A. Khare, E.S. Aydil, ACS Appl. Mater. Interfaces 3 (2011) 4444–4450.
[26] M.G. Ahmed, T.A. Kandiel, A.Y. Ahmed, I. Kretschmer, F. Rashwan, D. Bahnemann, J. Phys. Chem. C 119 (2015) 5864–5871.
[27] K. Maeda, D. Lu, K. Domen, ACS Catal. 3 (2013) 1026–1033.
[28] L.J. Zhang, S. Li, B.K. Liu, D.J. Wang, T.F. Xie, ACS Catal. 4 (2014) 3724–3729.
[29] H.J. Yun, H. Lee, N.D. Kim, D.M. Lee, S. Yu, J. Yi, ACS Nano 5 (2011) 4084–4090.
[30] H. Lin, J. Cao, B. Luo, B. Xu, S. Chen, Catal. Commun. 21 (2012) 91–95.
[31] R. Abe, K. Shinmei, N. Koumura, K. Hara, B. Ohtani, J. Am. Chem. Soc. 135 (2013) 16872–16884.
[32] E. Amstad, T. Gillich, I. Bilecka, M. Textor, E. Reimhult, Nano Lett. 9 (2009) 4042–4048.
[33] J. Miao, R.C. Pangule, E.E. Paskaleva, E.E. Hwang, R.S. Kane, R.J. Linhardt, J.S. Dordick, Biomaterials 32 (2011) 9557–9567.
[34] X. Fan, L. Zhang, M. Wang, W. Huang, Y. Zhou, M. Li, R. Cheng, J. Shi, Appl. Catal. B: Environ. 182 (2016) 68–73.
[35] H. Deng, B. Zhu, L. Song, C. Tu, F. Qiu, Y. Shi, D. Wang, L. Zhu, X. Zhu, Polym. Chem. 3 (2012) 421–428.
[36] J. Tian, L. Zhang, X. Fan, Y. Zhou, M. Wang, R. Cheng, M. Li, X. Kan, X. Jin, Z. Liu, Y. Gao, J. Shi, J. Mater. Chem. A 4 (2016) 13814–13821.
[37] K.-Y.A. Lin, J.-T. Lin, Chemosphere 182 (2017) 54–64.
[38] Y. Li, T. Tokizono, M. Liao, M. Zhong, Y. Koide, L. Yamada, J. Delaunay, Adv. Funct. Mater. 20 (2010) 3972–3978.
[39] P. Qiu, H. Chen, C. Xu, N. Zhou, F. Jiang, X. Wang, Y. Fu, J. Mater. Chem. A 3 (2015) 24237–24244.
[40] P. Qiu, C. Xu, H. Chen, F. Jiang, X. Wang, R. Lu, X. Zhang, Appl. Catal. B: Environ. 206 (2017) 319–327.
[41] J. Solomon, R. Madix, J. Stöhr, Surf. Sci. 255 (1991) 12–30.
[42] J. Tian, L. Zhang, X. Fan, Y. Zhou, M. Wang, R. Cheng, M. Li, X. Kan, X. Jin, Z. Liu, Y. Gao, J. Shi, J. Mater. Chem. A 4 (2016) 13814–13821.
[43] G. Dong, L. Yang, F. Wang, L. Zang, C. Wang, ACS Catal. 6 (2016) 6511–6519.
[44] B. Cheng, E.T. Samulski, J. Mater. Chem. 11 (2001) 2901–2902.
[45] J. Zhang, M. Zhang, C. Yang, X. Wang, Adv. Mater. 26 (2014) 4121–4126.
[46] S. Talapaneni, S. Anandan, G. Mane, C. Anand, D. Dhawale, S. Varghese, A. Mano, T. Mori, A. Vinu, J. Mater. Chem. 22 (2012) 9831–9840.
[47] W. Ho, Z. Zhang, W. Lin, S. Huang, X. Zhang, X. Wang, Y. Huang, ACS Appl. Mater. Interfaces 7 (2015) 5497–5505.
[48] Y. Chen, B. Wang, S. Lin, Y. Zhang, X. Wang, J. Phys. Chem. C 118 (2014) 29981–29989.
[49] M. Shalom, M. Guttentag, C. Fettkenhauer, S. Inal, D. Neher, A. Llobet, M. Antonietti, Chem. Mater. 26 (2014) 5812–5818.
[50] L. Perissinotti, M. Brusa, M. Grela, Langmuir 17 (2001) 8422–8427.
[51] N. Dimitrijevic, B. Vijayan, O. Poluektov, T. Rajh, K. Gray, H. He, P. Zapol, J. Am. Chem. Soc. 133 (2011) 3964–3971.
[52] L. Ye, J. Liu, Z. Jiang, T. Peng, L. Zan, Appl. Catal. B: Environ. 142 (2013) 1–7.